ADVANCED MATERIALS TECHNOLOGIES
www.advmattechnol.de

# Real-Time Monitoring of Cellular Barrier Functionality with Dynamic-Mode Current-Driven Organic Electrochemical Transistor

*Katharina Lieberth, Aristea Pavlou, Daria Harig, Paul W. M. Blom, Paschalis Gkoupidenis, and Fabrizio Torricelli**

**Cellular barriers control fundamental physiological functions in animals and plants. Accurate detection of barrier dysfunction requires real-time monitoring. Organic electrochemical transistors are a promising bioelectronic platform to monitoring cellular barriers. However, current approaches are not ideally suited for direct and real-time measurements: they require off-line model-based data analysis or slow measurement operation to achieve equilibrium conditions. Herein, dynamic-mode current-driven organic electrochemical transistors are proposed for direct real-time monitoring of cellular barrier functionality. In contrast to current approaches, the organic electrochemical transistor is operated under nonequilibrium conditions. The approach shows a sensitivity larger than $350 \times 10^{-6}$ V $(\Omega\ cm^2)^{-1}$ with an operating range of 13–640 $\Omega\ cm^2$. The sensitivity can be optimized on-line by simply changing the dynamic conditions and real-time monitoring of reversible barrier functionality is demonstrated by using a tight-junction modulator with a concentration as-low-as $122 \times 10^{-6}$ M. The theoretical foundation of the method is provided. The analysis shows the general applicability of the approach, opening opportunities for precision in vitro bioelectronics and medical diagnostic.**

## 1. Introduction

Cellular barriers are essential biological interfaces for the physiological functions of animals, humans, and plants, being able to control the transport of ions, small molecules, and nutrients through the separated compartments of a tissue. For instance, cellular barriers in plants contribute to the controlled uptake of water and mineral nutrients,[1,2] while in human body are the major building blocks of various organs, including, for example, skin, lungs, liver, kidney, and digestive track. The physiological function of the biological barriers is diverse among tissues and responds to the specific needs of each organ, including ion absorption, nutrients uptake, protection against toxins, and secretion of waste.[3,4]

Under normal physiological conditions the transcellular and paracellular pathways are finely regulated by the cellular barriers. Tight-junction (TJ) proteins—being responsible of the intercellular sealing—control the paracellular fluxes, providing either fully impermeable barriers or permeable-selective functions.[5–7] The permeability of TJs in a cell barrier can be regulated by physiological cues, can be modulated by drugs, and can be altered by various biological events such as inflammation, gastrointestinal tract diseases, cancer metastases, leukocyte migration, and viral infections. For instance, disruption of epithelial and endothelial barriers is a key clinical data differentiating patients with high probability to develop severe COVID-19 symptoms including the escalation in respiratory deficiency, loss of viral containment, and a progression toward multiorgan dysfunction.[8] Analogously, blood-brain barrier disruption contributes to the severity of diverse neurological diseases, including stroke, epilepsy, Alzheimer's disease, and multiple sclerosis, among others.[9,10] More in general, monitoring cellular barriers with noninvasive and label-free methods is relevant for in vitro studies,[11] for the development of organ-on-chip models,[12] for studying a disease progression, and for drug testing and drug targeting, also promoting the replacement for animal testing in toxicological profiling.[13]

So far, the integrity of cellular barriers has been addressed with transepithelial electrical resistance (TEER) measurements. TEER is an in vitro measurement technique based on two electrodes placed on each side of a cell layer. Upon the application of a direct or alternate current, the ionic impedance of the barrier layer is measured.[14] TEER direct current method is easy to perform and the measurement provides a resistance value that depends on both the cell status and the electrode positions. The positioning of the electrodes is performed manually, and this

K. Lieberth, A. Pavlou, D. Harig, P. W. M. Blom, P. Gkoupidenis
Max Planck Institute for Polymer Research
Ackermannweg 10, 55128 Mainz, Germany
F. Torricelli
Department of Information Engineering
University of Brescia
Via Branze 38, Brescia 25123, Italy
E-mail: fabrizio.torricelli@unibs.it
The ORCID identification number(s) for the author(s) of this article can be found under https://doi.org/10.1002/admt.202201697.



**DOI: 10.1002/admt.202201697**

results in lab-to-lab (operator dependent) large variability and limited scalability. By recording the ionic impedance at various frequencies, electrochemical impedance spectroscopy (EIS) provides a more accurate approach.[15,16] EIS is a well-established method for cell-layer status detection but unfortunately it requires time-consuming measurements and modeling, which limit the time resolution and increase the complexity. In addition, EIS measurements are based on small-amplitude signals, typically in the range of few millivolts, and a suitable signal-to-noise ratio demands additional filtering and amplification operations, which increase the complexity of the experimental set-up and the cost of the equipment.[17]

In recent years, organic electrochemical transistors (OECTs) have been proposed as an effective alternative approach to electrically assess cellular barrier properties.[18,19] OECTs are three-terminal iontronic devices where the electronic conductivity of an ionic–electronic conducting polymer, connected by two electrodes named source and drain, is modulated by a third electrode, named gate. The gate and the channel are in direct contact with an electrolyte and the polarity and magnitude of the applied gate voltage ($V_G$) give rise a drift of anions or cations from the electrolyte to the channel and vice versa.[20–24] When an OECT is used to measure a barrier tissue, the biological barrier can be placed in-between the gate and the channel. In this configuration, the ion transport depends on the barrier status that, in turn, is mirrored by the electrical characteristics of the OECT. The pioneering work of Owens and co-workers,[17] demonstrated the application of an OECT as a sensor for barrier tissue by applying a pulsed $V_G$ and measuring the drain–source current $I_D$. This approach is suitable for long-term measurements but requires a model-based analysis of the recorded characteristics.[25–27] To avoid the need of postprocessing, Hsing and co-workers proposed the direct coupling of cells' physiological ionic current.[28] This approach was further optimized by Iannotta and co-workers that, focusing on the detection of irreversible barrier disruption, proposed the use of water as low ion concentration basal electrolyte but, unfortunately, a model-based analysis was re-introduced.[29]

To monitor the reversible barrier functionality without the requirement of modeling and postprocessing analysis, we recently proposed the current-driven OECT configuration.[30,31] This method can assess the integrity of cellular barriers when toxic compounds (e.g., $H_2O_2$) at a concentration of $10^{-3}$ M are added to the cell media. Very recently, using the same approach and optimizing the design in equilibrium conditions, we demonstrated the monitoring of reversible TJ modulations.[32] Under equilibrium conditions the hysteresis in the electrical characteristics is minimized, avoiding a multivalued current when the same gate bias is applied. This is currently considered a stable measurement condition and provides a direct interpretation of the results.[33–35] To minimize the hysteresis small device geometries and/or slow scan rate are required. Unfortunately, small device geometries are not an optimal design solution for the high-sensitivity monitoring of the cellular membranes[31,36] while slow scan rates lead to large measurement time that, in turn, results in low time resolution. Therefore, while OECTs are a promising bioelectronic technology for the in vitro investigation of the cellular barrier functionalities, current approaches are not ideally suited for the real-time monitoring.

Here we propose real-time monitoring of cellular barrier functionality with dynamic-mode current-driven OECTs. In contrast to the current approaches, the OECT is deliberately operated under nonequilibrium hysteretic conditions. The dynamic-mode current-driven OECT enables cellular barrier monitoring with a sensitivity of $350 \times 10^{-6} \pm 10 \times 10^{-6}$ V $(\Omega\ \text{cm}^2)^{-1}$ and an operating range of 13–640 $\Omega\ \text{cm}^2$, extending from intact and high-resistivity to fully disrupted and low-resistivity biological barriers. The output sensitivity can be enhanced on-line and in real-time directly during the experiments, allowing the real-time monitoring of reversible TJs modulation using a modulator concentration as low as $c = 122 \times 10^{-6}$ M. The theoretical foundation of the proposed approach is explained by means of numerical simulations. Importantly, we highlight that the model-based simulations are essential to gain insight on the proposed method but are not needed for its practical application. The ultralow detection-limit combined with high-sensitivity and wide-range makes this approach a suitable technology for accurate monitoring subtle variations of barrier functionality.

## 2. Results and Discussion

### 2.1. Dynamic-Mode Current-Driven Organic Electrochemical Transistor

The current-driven OECT configuration integrating a barrier tissue is displayed in **Figure 1**a. In this configuration the OECT is connected in series with a current generator setting a bias current $I_B$. The output voltage $V_O$ is measured at the drain and the input voltage $V_I$ is applied to a Ag/AgCl quasi-reference electrode. A Transwell filter with a barrier tissue is placed in-between the quasi-reference electrode gaiting the OECT and the polymeric channel, thus separating the electrolyte into two compartments. The prototypical ionic–electronic conductive polymer poly(3,4-ethylenediox-ythiophene) doped with poly(styrene sulfonate) (PEDOT:PSS) is used for the OECT channel. PEDOT:PSS has been proven to be very stable in liquid environment even when in direct contact with the cell culture medium, thus ensuring the ideal biological conditions.[37–39] The equivalent electronic circuit of the current-driven OECT embedding the Transwell filter with a biological membrane is displayed in Figure 1b. Specifically, $R_A$ describes the nonpolarizable gate electrode and the ionic resistance due to the ion transport through the apical electrolyte, the barrier tissue membrane is modeled by a resistor $R_M$ in parallel to a capacitor $C_M$, and $R_F$ and $R_B$ describes the ionic resistance of the Transwell filter and of the basal electrolyte, respectively. We note that $R_M$ accounts for the ion transport through the cellular membrane while $C_M$ models the ion accumulation at the apical and basal membrane interfaces.[19] The aforementioned parameters are experimentally obtained by means of EIS measurements, as detailed in Figure S1 of the Supporting Information. To probe the impedance of the cellular barrier, the experimental set-up should guarantee that $Z_{M\text{-}i} >> (R_A + R_{FILTER} + R_B)$, where $Z_{M\text{-}i}$ is the impedance of the intact cell barrier. The OECT channel is described considering the ionic–electronic volumetric capacitance and the charge transport in the electronic channel. The

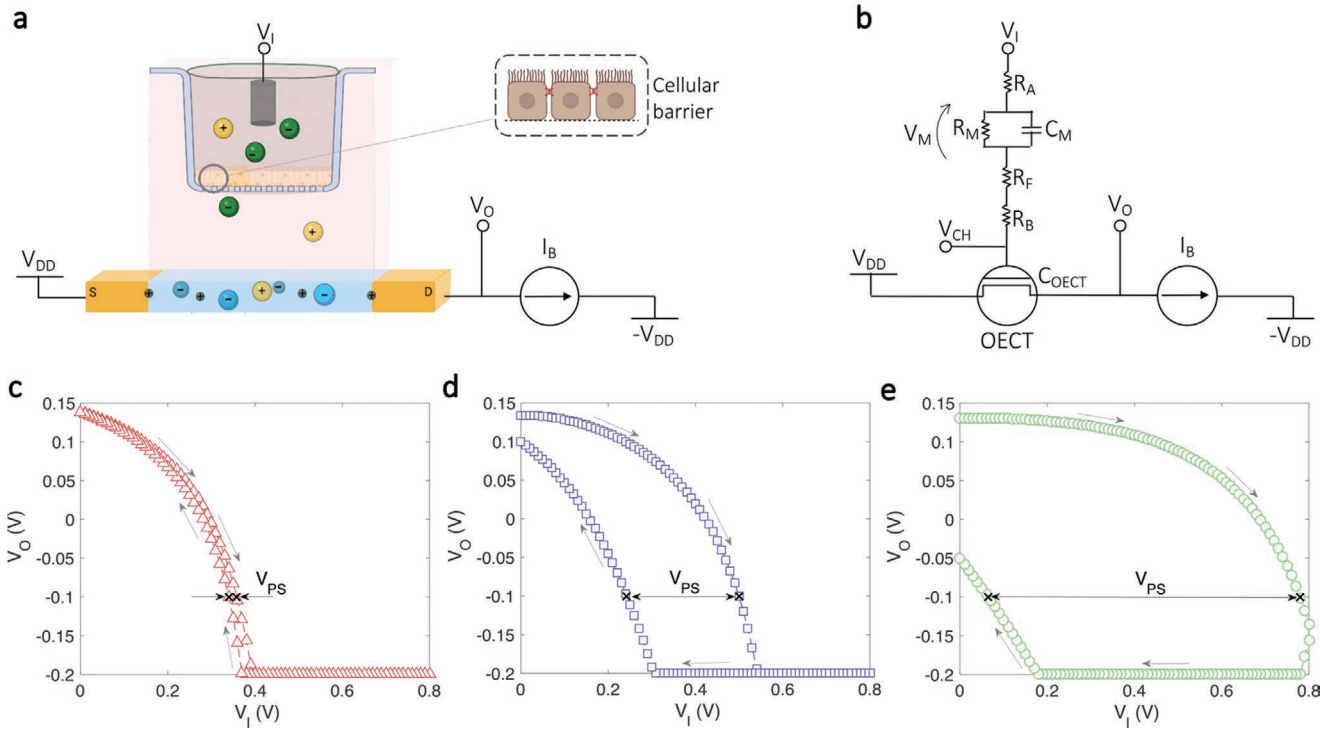


**Figure 1.** Dynamic-mode current-driven organic electrochemical transistor (OECT). a) Current-driven OECT configuration coupled with a biological barrier. The cellular barrier tissue is seeded in a Transwell filter and cell medium is used as electrolyte. The gate electrode is immersed in the apical compartment and the OECT channel is in contact with the basal compartment. The ion transport between the two compartments depends on the status of the barrier tissue. Created with BioRender.com. b) Equivalent circuit model of a dynamic-mode current-driven OECT coupled with a biological barrier tissue. The barrier tissue is described with a resistor $R_M$ in parallel to a capacitor $C_M$. $R_M$ accounts for the ion transport across the barrier and $C_M$ models the ion accumulation at the apical and basal barrier interfaces. $R_A$ and $R_B$ are the ionic resistance of the apical and basal electrolyte, respectively. $R_F$ is the ionic resistance of the Transwell filter and $C_{OECT}$ is the overall capacitance of the OECT polymeric channel. $V_I$ is the input voltage, $V_{CH}$ is the voltage actually gating the OECT, $V_{DD}$ is the supply voltage, $I_B$ is the bias current, and $V_O$ is the output voltage. The gray arrows show the forward and backward scans. c) Typical transfer characteristic $V_O$–$V_I$ of a dynamic current-driven OECT operated at a scan rate SR = 0.002 V $s^{-1}$. The phase-shift voltage $V_{PS}$ is displayed. d) Measured $V_O$–$V_I$ at SR = 0.15 V $s^{-1}$. e) Measured $V_O$–$V_I$ at SR = 0.5 V $s^{-1}$. The gate is a Ag/AgCl pellet, the OECT geometries are: $W = 2$ mm, $L = 1$ mm, thickness $t = 300$ nm. $I_B = 5 \times 10^{-3}$ A and $V_{DD} = 0.2$ V.

OECT parameters are extracted by modeling the transfer and output characteristics, as displayed in Figure S2 of the Supporting Information. In the following, the model depicted in Figure 1b will be used only to systematically understand the fundamentals of operation and model-based data analysis is not required for operation.

The idea is to monitor the status of the cellular barrier taking advantage of the transient response of the ionic–electronic biological system. A typical transfer characteristic ($V_O$–$V_I$) of the dynamic-mode current-driven OECT integrating a cellular barrier is displayed in Figure 1c. The input voltage $V_I$ is swept forward and backward, from 0 to 0.8 V and back to 0.8 V, and the corresponding output voltage $V_O$ is measured. When $V_I$ is swept with a slow scan rate (i.e., by ensuring quasi-equilibrium conditions), e.g., SR = 0.002 V $s^{-1}$ in Figure 1c, the forward and backward characteristics are almost perfectly overlapped. More in detail, when $V_I = 0$ V the p-type OECT is highly conductive and pulls-up the output voltage, resulting in $V_O = +V_{DD}$. By increasing the input voltage $V_I$, the OECT channel resistance ($R_{OECT}$) increases, $I_B$ is set by the current generator, the voltage drop on the OECT channel ($V_{SD} = R_{OECT}\ I_B$) increases and, as a consequence, $V_O = V_{DD}$–$R_{OECT}\ I_B$ reduces. Further increasing $V_I$, the switching voltage $V_{SW}$ is achieved ($V_{SW} = 0.39$ V in Figure 1c), the OECT operates in saturation, and $V_O$ is pulled-down to the minimum supply voltage ($V_O = -V_{DD}$). By increasing the scan rate of the input voltage, dynamic-mode conditions are obtained. Under these conditions the forward and backward characteristics do not overlap anymore and, as displayed in Figure 1d,e, the $V_O$–$V_I$ characteristic shows a hysteretic loop. The switching voltage of the forward characteristic ($V_{SWf}$) is larger than the switching voltage of the backward characteristic ($V_{SWb}$) and the voltage difference $V_{PS} = V_{SWf}$–$V_{SWb}$ increases by increasing SR. For instance, when SR = 0.15 V $s^{-1}$ (Figure 1d). $V_{SWf} = 0.50$ V, $V_{SWb} = 0.24$ V, and $V_{PS} = 0.26$ V, which increases to $V_{PS} = 0.72$ V when SR = 0.5 V $s^{-1}$ (Figure 1e). It is worth to note that $V_{PS}$ is calculated at $V_O = -0.1$ V because the output voltage $V_O = -0.13$ V at the maximum $V_I$ and SR of the forward scan (Figure 1e). In general $V_{PS}$ can be extracted at $V_O \geq V_{Omin(fw)}$, where $V_{Omin(fw)}$ is the minimum $V_O$ of the forward scan.

This can be explained as follows. In the dynamic-mode current-driven OECT configuration, a triangular waveform with amplitude $V_I$ and frequency $f_I$ is applied as input. The frequency $f_I$ is modulated by SR and reads: $f_I = SR \times (V_{max}$–$V_{min})^{-1}$, where $V_{max}$ and $V_{min}$ are the maximum and minimum amplitude of $V_I$, respectively. In our case $V_{min} = 0$ V and

$V_{max}$ = 0.8 V (Figure 1c–e). Considering the circuit model in Figure 1b, the amplitude and phase of the voltage actually gaiting the OECT channel, named $V_{CH}$, depends on the input frequency $f_I$ and on the time-response of the *R*–*C* circuit accounting for the impedance of the cellular barrier ($R_M$, $C_M$), the electrolyte resistances ($R_A$ and $R_B$), the Transwell filter resistance ($R_F$) and the OECT capacitance ($C_{OECT}$). A detailed calculation is provided in Note S1 of the Supporting Information.

### 2.2. Operation Mechanism

To gain insight on the operation of the dynamic-mode current-driven OECT configuration embedding a cellular barrier, we implemented the equivalent circuit displayed in Figure 1b in a numerical simulator accounting for the physical parameters obtained from the EIS, $I_D$–$V_G$, and $I_D$–$V_D$ measurements (Figures S1 and S2, Supporting Information). We note that a linear analysis cannot be applied because $V_I$ is a large-signal triangular wave, and the current-driven OECT gives rise to a nonlinear input–output characteristic ($I_D$–$V_{CH}$). As a consequence, numerical nonlinear simulations are required. We highlight that the simulations are relevant to understand the bioelectronic system fundamentals but are not required when operating the system. As displayed in **Figure 2**a, the simulations accurately predict the measurements in the whole range of $V_I$ and SR. More in detail, we calculated the transient responses as a function of SR. For the sake of clarity, the various time responses are normalized to the corresponding SR. Figure 2b–e shows the input voltage ($V_I$), the potential drop across barrier tissue ($V_M$), the actual potential gating the OECT ($V_{CH}$), and the output voltage ($V_O$) as a function of the number of periods $N_P$ = SR × total time × $((V_{max}–V_{min}) × 2)^{-1}$. When SR = 0.002 V s$^{-1}$, $V_M$ is negligible (Figure 2c, red line), $V_{CH}$ shows the same amplitude and phase of $V_I$ (**Figure 3**d, red line), and the forward and backward $V_O$–$V_I$ characteristics are almost overlapped (Figure 2a, red line). Therefore, for low SRs the cellular membrane is practically not probed. By increasing the scan rate at SR = 0.15 V s$^{-1}$, the impedance of the OECT decreases, the voltage drop on the cellular membrane increases at about $V_M \approx 0.2$ V and the $V_M$ oscillation has almost the same phase of the input signal $V_I$ (Figure 2c, blue line). Conversely, $V_{CH}$ is attenuated and shifted with respect to $V_I$ (Figure 2d, blue line) and, as displayed in Figure 2e (green line), this is mirrored in a phase-shift of $V_O$. This behavior is confirmed by further increasing the scan rate at SR = 0.5 V s$^{-1}$. In this condition, $V_M \approx 0.6$ V (Figure 2c, green line), $V_{CH}$ is significantly attenuated and shifted with respect to $V_I$, and the corresponding $V_O$ shows an increased phase-shift (Figure 3e, green line). As a result, the cellular membrane is probed for high SRs. Focusing on the amplitude of $V_O$, the maximum output voltage slightly decreases at the maximum SR while

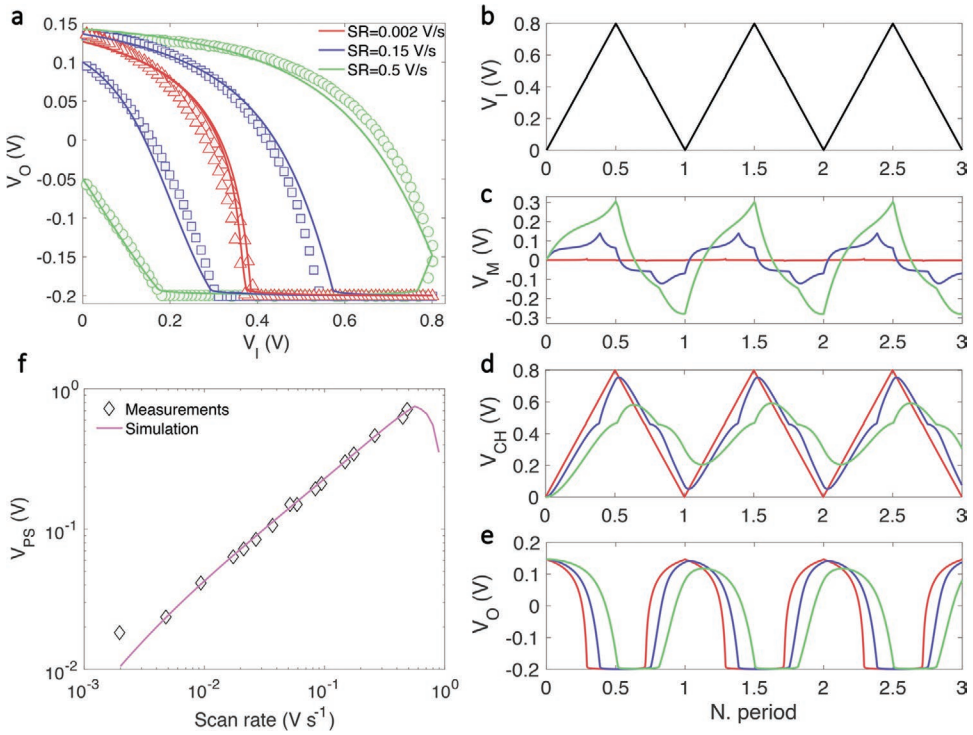


**Figure 2.** Operation mechanism. a) Measured (symbols) and model (lines) transfer characteristics ($V_O$–$V_I$) as a function of the scan rate SR = 0.002 V s$^{-1}$ (triangles), SR = 0.15 V s$^{-1}$ (squares), and SR = 0.5 V s$^{-1}$ (circles). b–e) Simulations of dynamic-mode current-driven OECT with a cellular barrier at various SR:SR = 0.002 V s$^{-1}$ (red line), SR = 0.15 V s$^{-1}$ (blue line), and SR = 0.5 V s$^{-1}$ (green line). Applied input voltage $V_I$, calculated voltage across the cellular barrier $V_M$, channel voltage $V_{CH}$, and output voltage $V_O$ as a function of time normalized to the input frequency, number of period $N_P$ = time $(V_{max}–V_{min})$ SR$^{-1}$, where $V_{max}$ and $V_{min}$ are the maximum and minimum applied input voltage. Scan rate: SR = 0.002 V s$^{-1}$ (red line), SR = 0.15 V s$^{-1}$ (blue line), and SR = 0.5 V s$^{-1}$ (green line). f) Phase-shift voltage $V_{PS}$ as a function of the scan rate SR. Symbols are the measurements and line is calculated with the numerical simulations. Applied bias conditions: $I_B = 5 \times 10^{-3}$ A and $V_{DD} = 0.2$ V.

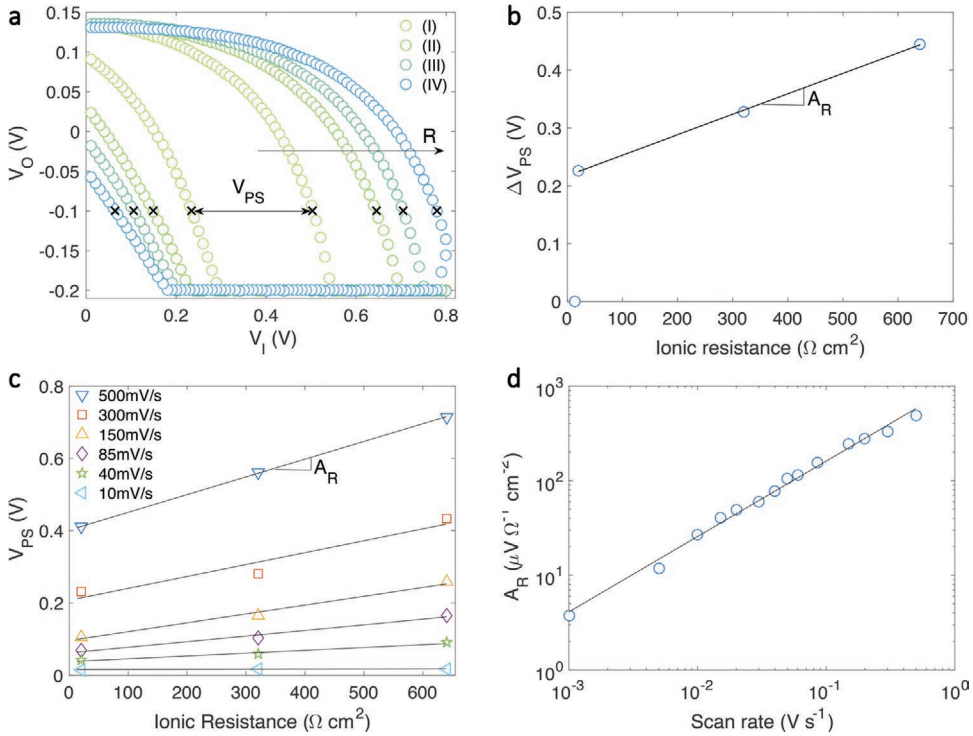


**Figure 3.** Dynamic reconfiguration of the performance. a) Transfer characteristics ($V_O$–$V_I$) measured as a function of ionic resistance $R$. Four relevant experimental cases are considered: (I) cell medium $R = 13\ \Omega\ cm^2$, (II) cell medium with Transwell filter $R = 20\ \Omega\ cm^2$, (III) low-resistance cellular barrier $R = 320\ \Omega\ cm^2$, and (IV) high-resistance cellular barrier $R = 640\ \Omega\ cm^2$. Considering the model displayed in Figure 1b, $R = R_A + R_M + R_F + R_B$. In all cases SR = 0.5 V s$^{-1}$. The cross symbols indicate the forward and backward switching voltage for the various cases and, as an example, the phase-shift voltage $V_{PS}$ is explicitly shown in the case (I). b) Variation of the phase-shift voltage $\Delta V_{PS} = V_{PS}–V_{PS(I)}$ as a function of the ionic resistance $R$. $V_{PS(I)}$ is $V_{PS}$ obtained in the reference case (I). SR = 0.5 V s$^{-1}$. Full line is the linear least square fit to the measurements and yields a sensitivity to the ionic resistance $A_R = (350 \pm 10) \times 10^{-6}$ V $(\Omega\ cm^2)^{-1}$. c) Measured $V_{PS}$ as a function of the ionic resistance $R$ by varying SR showing that $A_R$ consistently increases by increasing SR. d) Calculated average $A_R$ as a function of SR. Applied bias conditions: $I_B = 5 \times 10^{-3}$ A and $V_{DD} = 0.2$ V.

the minimum output voltage is not altered ($V_{Omin} = -V_{DD}$, $V_{DD} = 0.2$ V).

This behavior is inherently due to the OECT current-driven configuration: the pull-up toward $V_{DD}$ depends on the overdrive voltage $V_{DD}–V_{CH}$ applied to the OECT, while the output pull-down toward $-V_{DD}$ is achieved by means of the current generator $I_B$. As a result, in a dynamic-mode current-driven OECT the voltage $V_{PS} = V_{SWf}–V_{SWb}$ is related to the input–output phase shift, providing a direct measurement of the ionic resistance of the cellular barrier. Indeed, as displayed in Figure S3 of the Supporting Information this hysteretic behavior disappears when the $V_O–V_{CH}$ characteristics are plotted, confirming that $V_{PS}$ provides information on the status of the barrier tissue. Interestingly, the provided analysis indicates that the sensitivity can be enhanced by means of SR. Figure 2f shows the measured $V_{PS}$ (symbols) as a function of SR. $V_{PS}$ systematically increases by increasing SR in the range $2 \times 10^{-3}$–$5 \times 10^{-1}$ V s$^{-1}$. At SR = 0.5 V s$^{-1}$ we obtained $V_{PS} = 0.72$ V, which is equal to 90% of the maximum input voltage. Overall, the dynamic-mode current-driven OECT shows a scan-rate sensitivity equal to 1391 mV V$^{-1}$ s. The simulations (Figure 2f, full line) accurately predict the measurements showing that the maximum performance is achieved. Indeed, further increasing SR the voltage drop on the cellular barrier increases as well, resulting in a decreasing of $V_{CH}$. As a consequence, although the phase-shift increases, the OECT current reduces eventually resulting in a smaller $V_{PS}$ (Figure S4, Supporting Information).

### 2.3. Operating Range

To experimentally investigate the operating range of the dynamic-mode current driven OECT, the ionic resistance between the gate and the channel is systematically varied considering four relevant cases: I) cell medium electrolyte only ($R = 13\ \Omega\ cm^2$), II) cell medium with Transwell filter ($R = 20\ \Omega\ cm^2$), III) low-resistance barrier ($R = 320\ \Omega\ cm^2$), and IV) high-resistance barrier ($R = 640\ \Omega\ cm^2$). We note that this range of resistances covers the relevant biological conditions, including intact and fully disrupted barrier tissues as well as the bare experimental set-up. Figure 3a shows the corresponding $V_O–V_I$ measurements when SR = 0.5 V s$^{-1}$. $V_{PS}$ consistently increases by increasing the ionic resistance $R$. To quantitatively evaluate the effect of the ionic resistance on $V_{PS}$, we calculated $\Delta V_{PS} = V_{PS}–V_{PS(I)}$ where $V_{PS(I)}$ is the value of $V_{PS}$ obtained in the reference case (I) where only the electrolyte is used. Figure 3b shows $\Delta V_{PS}$ as a function of ionic resistance $R$. $V_{PS}$ increases by a factor of two in the experimental range we assessed. More in detail, by inserting the Transwell filter into the electrolyte, $R$ increases from 13 to 20 $\Omega\ cm^2$ resulting in a $\Delta V_{PS} = 226.2$ mV. $\Delta V_{PS}$

increases to 327.8 mV when Transwell filter with a confluent barrier tissue of "low-resistance" Caco-2 cell line is measured and $R = 320\ \Omega\ cm^2$. $\Delta V_{PS} = 445.3$ mV when Transwell filter with "high-resistance" Caco-2 cells is measured and $R = 640\ \Omega\ cm^2$. The least-square linear approximation of the measured $\Delta V_{PS}$ as a function of $R$ (Figure 3b) yields an average sensitivity $A_R = dV_{PS}/dR = 350 \times 10^{-6} \pm 10 \times 10^{-6}$ V $(\Omega\ cm^2)^{-1}$. We note that case (I) is very relevant for evaluating the experimental set-up but it is of limited practical interest when monitoring the barrier tissues and therefore, to be conservative, it was not considered in the calculation of sensitivity. The dynamic-mode current-driven OECT shows an operating range of 13–640 $\Omega\ cm^2$, which is relevant to assess both fully disrupted and intact cellular barriers. Indeed, the characteristic TER range for confluent Caco-2 cell barrier is 140–700 $\Omega\ cm^2$.[31,40–42] For instance, Tria et al. showed that the TER-value decreases to 20% of its initial value when Caco-2 cells are exposed to 10 mM EGTA,[43] and Ramuz et al. demonstrated that TER-values below 100 $\Omega\ cm^2$ are typical of tissues without barrier function, whereas a TER from 100 to 300 $\Omega\ cm^2$ is obtained in the case of a partial barrier function.[44]

To further assess the effectiveness of the proposed approach, we measured the $V_O$–$V_I$ input–output characteristics as a function of ionic resistance at various SR. Figure 3c shows that $V_{PS}$ monotonically increases with $R$ and the sensitivity $A_R$ systematically increases by increasing SR. More in detail, the phase-shift between the input signal $V_I$ and the voltage $V_{CH}$ becomes larger at faster SR. The enhanced sensitivity to the ionic resistance $R$ results in a larger $V_{PS}$. This is confirmed in Figure 3d where $A_R$ as a function of SR is displayed. When the scan rate is very slow, $V_{CH} = V_I$, the signals show the same amplitude and phase, and it is not possible to detect the barrier status. By contrast, at high SR, e.g., SR = 0.5 V $s^{-1}$, a large $V_I$–$V_{CH}$ phase shift is obtained because of the voltage partition between the ionic impedance of the barrier tissue and the ionic–electronic volumetric capacitance of the polymeric channel. This voltage partition is eventually converted in a large variation of $V_{PS}$ by the dynamic-mode current-driven OECT. These results are further corroborated in Figure S5 of the Supporting Information, showing that the measured $V_{PS}$ depends on $R$ and the sensitivity can be significantly enhanced by means of SR.

### 2.4. Real-Time Monitoring of Cellular Barrier Functionality

As a relevant application, high-sensitivity real-time monitoring of cellular barrier functionality is demonstrated. As a model system, we used confluent barrier tissue of the Caco-2 cell line. Caco-2 cells are widely used as a model of intestinal barrier permeability, which is the major barrier separating our body from the external environment and it is essential to avoid any imbalance in homeostasis.[45,46] For instance, an imbalance in the intestinal barrier can give rise to an uncontrollable immune reaction or various diseases including inflammatory disorders, rheumatoid arthritis, and metabolic disorders, e.g., obesity and diabetes.

As a first step, the dynamic-mode current-driven OECT approach is benchmarked with the state-of-art OECT approaches including transient response OECT measurements and conventional current-driven OECT.[36,47] As displayed in **Figure 4**a, the cell media is used as electrolyte and the electronic response is measured when a bare Transwell filter and a transwell filter with intact Caco-2 cell barrier are embedded in the current-driven OECT configuration. The OECT transient response and current-driven architectures are measured in the very same conditions, viz. same barrier and consequently. To directly compare the various architectures, we calculated the normalized output response $NR = 100 \times (OR–OR_0)/OR_0$, where in the case of transient response OR and $OR_0$ is the transient time with and without cells, respectively, in the case of conventional current-driven OR and $OR_0$ is the switching voltage $V_{SW}$ measured with and without cells, respectively, and in the case of dynamic-mode current-driven OECT OR and $OR_0$ is the phase-shift voltage $V_{PS}$ measured with and without cells, respectively. Figure 4b shows NR as a function of time for the various methods. The insertion of the cell barrier results in an NR > 120% in the case of dynamic-mode current-driven (DCD) OECT operated at SR = 0.5 V $s^{-1}$. NR reduces to 40% when the conventional current-driven (CD) is used and lowers to NR = 25% in the case of the transient response method. This comparison shows that DCD provides an enhanced sensitivity with respect to the state-of-art OECT methods.

As a next step, cellular barrier functionality is monitored in real-time and in the very same biological conditions with the DCD and CD approaches. The relevant transfer characteristics $V_O$–$V_I$ measured with a DCD-OECT as a function of time are displayed in Figure 4c. The DCD-OECT with the intact barrier shows perfectly overlapped characteristics after 3 and 4 h of continuous measurements, proving the excellent stability of the bioelectronic system. Then, the barrier tissue is exposed to a low concentration of poly-L-lysine (PLL) TJ modulator, $c_{PLL} = 122 \times 10^{-6}$ M, and after ≈1.5 h form the PLL modulator addition the TJs are opened (barrier disrupted). Ions can transport from the apical to the basal electrolyte compartment and vice-versa passing through the open channels of the cell barrier. The forward and backward characteristic shifts to smaller and larger $V_I$, respectively, and as a consequence the phase-shift voltage $V_{PS}$ reduces. Then, the electrolyte cell media with PLL is exchanged (i.e., PLL is removed), the cellular barrier recovers, the $V_O$–$V_I$ characteristics shift back, and the corresponding $V_{PS}$ increases. After 7 h upon medium replacement, cellular recovery is completed (Figure 4c, green line). A comparison with the initial characteristic of the intact barrier (blue line) suggests that a small amount of TJs could be still opened and a fully recovery after PLL exposure could not be achieved.

As a comparison, real-time monitoring of the barrier functionality with DCD and CD are displayed in Figure 4d. We note that DCD and CD require the very same experimental set-up, without performing manual operations during the whole time of the measurements. The output voltage $V_{PS}$ and $V_{SW}$ are normalized with respect to their value obtained when the barrier is intact ($t = t_0$, and $t_0 = 3$ h in Figure 4d), before exposure to PLL, and hence $\Delta V_{PS} = V_{PS}(t)–V_{PS}(t_0)$ and $\Delta V_{SW} = V_{SW}(t)–V_{SW}(t_0)$. The comparison of $\Delta V_{PS}$ and $\Delta V_{SW}$ as a function of barrier status demonstrates the real-time high sensitivity of the DCD. Indeed, CD shows a very limited response because of the very small concentration of PLL. By contrast, in the very same biochemical conditions the DCD architecture provides a response $\Delta V_{PS}$ of up to 216.2 mV and both the opening and

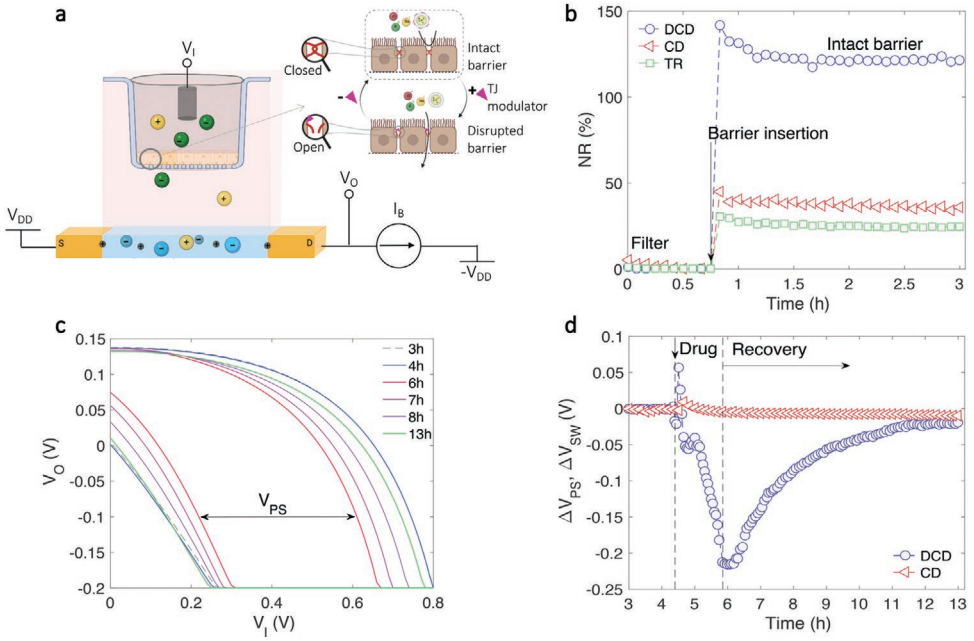


**Figure 4.** Real-time monitoring of cellular barrier functionality. a) Schematic representation of a current-driven OECT coupled with a biological barrier tissue, e.g., human Caco-2 cells. Ion transport through the barrier depends on the status of the tight junctions (TJs) proteins. Upon to the addition of a TJ modulator, inserted on a drug carrier, TJs open, the tissue becomes permeable to ions and drug carriers. By removing the TJ modulator in the electrolyte, the TJs are closed and the barrier functionality is restored limiting the ions and drug passage. Created with BioRender.com. b) Normalized response NR = 100 × (OR–$OR_0$)/$OR_0$ as a function of time. In the case of transient response OR and $OR_0$ is the transient time with and without cells, respectively, in the case of conventional current-driven (CD) OR and $OR_0$ is the switching voltage $V_{SW}$ measured with and without cells, respectively, and the case of dynamic-mode current-driven (DCD) OECT OR and $OR_0$ is the phase-shift voltage $V_{PS}$ measured with and without cells, respectively. The cell barrier is inserted into the electrolyte at time = 50 min and then the intact barrier is monitored for more than 2 h. c) Transfer characteristics ($V_O$–$V_I$) measured as a function of time. The intact barrier is measured two times at time $t$ = 3 h and $t$ = 4 h. Then the TJ modulator PLL, $c_{PLL} = 122 \times 10^{-6}$ M, is added to the cell medium. The measured barrier status is displayed at time = 6 h where a large amount of TJs are open. Then the electrolyte cell media with PLL is exchanged, and the $V_O$–$V_I$ characteristics at $t$ = 7, 8, 13 h show the recovery of the cellular barrier. d) Output signal measured with a DCD, $\Delta V_{PS} = V_{PS}(t)–V_{PS}(t_0)$, and CD, $\Delta V_{SW} = V_{SW}(t)–V_{SW}(t_0)$, as a function of time. The initial time is $t_0$ = 3 h. The CD shows a limited response because of the very small concentration of PLL. By contrast, the dynamic current-driven OECT provides a response $\Delta V_{PS}$ of up to 216.2 mV and both the disruption and recovery temporal dynamics are recorded in real-time and high sensitivity. The introduction of the filter with the barrier layer (panel b) and the PLL injection into the electrolyte (panel d) give rise to a fluid mixing that, for a limited period of time upon the perturbation, results in an increase of the ion mobility. The temporary increase of the ion mobility is mirrored by a spike of the $V_{PS}$.

recovery temporal dynamics can be recorded. To further assess the stability of the DCD experiments, we measured a Caco-2 cell barrier without any stress. More in detail, the DCD with a filter without the barrier is measured for ≈1 h. Then, the bare filter is replaced with a filter including a cell barrier. The DCD with cell barrier is measured for ≈12 h without any stress. The measured $\Delta V_{PS}$ as a function of time is shown in Figure S6 of the Supporting Information. The insertion of the filter with the barrier layer gives rise to a fluid mixing that results in an increase of the ion mobility and is mirrored by a peak of $\Delta V_{PS}$. This is in full agreement with the results displayed in Figure 4d. After ≈20 min, the output signal $\Delta V_{PS}$ reaches a plateau and remains stable for the whole time of the experiment (≈11.5 h). We note that the maximum variation of the output signal amounts to $\Delta V_{PS}(t = 13\text{ h})–\Delta V_{PS}(t = 1.5\text{ h}) = 0.01$ V, which is negligible compared to the signal variation measured during barrier disruption and recovery (>0.2 V, Figure 4d). Finally, we note that the time period of our experiments (≈12 h) is suitable for acute toxicology or diagnostics purposes and, in agreement with previous studies,[30,32,48,49] over this period of time we did not find a significant impact of the Ag/AgCl electrode.

## 3. Conclusion

Seeking for bioelectronic alternatives replacing the animal model on the in vitro platform, we proposed the dynamic-mode current-driven OECT configuration for high-sensitivity real-time monitoring of the cellular barrier functionality. This approach provides a direct real-time measurement of the cellular barrier status, with on-line reconfiguration and optimization of the bioelectronic system parameters.

The rational and operating principles of the proposed approach are investigated by means of numerical simulations, highlighting the key design parameters. Neither hardware post-processing analysis nor multiple-cycle design-optimization phases are required. The sensitivity can be dynamically reconfigured during the operation by simply changing the scan rate of the input signal, achieving optimal system performance in the whole range of biological conditions. A maximum sensitivity equal to 1391 mV $V^{-1}$ s is demonstrated.

The experimental analysis of the DCD-OECT provided an average ionic resistance sensitivity equal to $350 \times 10^{-6} \pm 10 \times 10^{-6}$ V $(\Omega\ cm^2)^{-1}$ with an operating range of 13–640 Ω $cm^2$.

The high sensitivity combined with the direct output response and easy reconfiguration even during the real-time operation, allowed us to accurately monitor barrier disruption and recovery in human Caco-2 cells using PLL modulator at a concentration down to $122 \times 10^{-6}$ M. The DCD approach is benchmarked under the very same biochemical conditions with the CD approach, highlighting the superior performance of the DCD-OECT method.

Prospectively, the proposed approach could be used as-it-is for real-time multiparametric in vitro cell monitoring including cell layer coverage, cellular vitality, differentiation, ionic channel molecular transport, and cell toxicity experiments. In addition, the proposed technological implementation can be extended to other electrochemical transistor material technologies including, for example, n-type and ambipolar organic mixed ionic–electronic conductors, as well as accumulation and depletion mode OECTs.[35,50–53] Overall, the high sensitivity combined with the reconfigurable operation and simple fabrication on flexible or even conformable substrates can open opportunities for next-generation organic bioelectronics.

## 4. Experimental Section

*Device Fabrication*: Glass substrates were cleaned by sonication in DI water with soap (Micro-90) and in a 1:1 (vol/vol) solvent mixture (acetone, isopropanol), followed by drying and UV ozone cleaning. Gold source and drain electrodes with chromium as an adhesion layer (5 nm) were deposited by thermal evaporation using a shadow mask for defined channel dimensions ($W$ = 2 mm, $L$ = 1 mm). The PEDOT:PSS formulation consisted of an aqueous dispersion of the conducting p-type polymer PEDOT:PSS (Clevios PH1000), mixed with 5 vol% ethylene glycol, 0.1 vol % dodecyl benzene sulfonic acid, and 1 vol% (3-glycidyloxypropyl) trimethoxysilane)], and spin-coated first at 1500 rpm and then two times at 650 rpm for 60 *s* with an annealing step of 120 °C for 1 min in between the first two steps. The devices were baked 1 h at 140 °C, then glass slides were soaked in DI water for 1 h. To contain the electrolyte, a polymethyl methacrylate-well was placed on top of the device using double-sided tape.[54,55]

*Device Measurements*: All electrical measurements were performed in a humified atmosphere with 5% $CO_2$ by using a Keithley 4200-Semiconductor Characterization System and were analyzed by using OriginLab software. Cell culture medium (Eagle's minimum essential medium, EMEM) was utilized as an electrolyte apical and basal. A Ag/AgCl electrode (pellet, 2 mm, Warner Instruments) operated as a gate, was immersed in the Transwell filter. The operating gate voltage was kept well below 1.0 V to avoid water electrolysis and any cell damage. For the dynamic current-driven configuration a dual sweep of the input voltage $V_{IN}$ = [0; 0.8] $V$ was performed at the gate. The scan speed was chosen in the range of [0.002; 0.5] V $s^{-1}$. For the standard current-driven measurement the input voltage was swept forward only and the scan rate SR = 0.125 V $s^{-1}$. The supply voltage was kept same for both techniques at $V_{DD}$ = 0.2 V. For transient response measurements $V_G$ was pulsed at 0.5 V ($t_{OFF}$ = 3 min, $t_{ON}$ = 15 s) and $V_D$ was kept constant at $V_D$ = –0.2 V. These parameters are in agreement with previous studies.[26,30,56] The transient response time was extracted by an exponential fit of $I_D(t)$ using the following equation: $I_D = A_1 \exp(-t/\tau_1) + I_{D0}$, where $\tau_1$ is the dominant time constant. A single exponential model where the time constant $\tau_1$ accounts for the device response time influenced by the cell layer status was used.[26,30,36,48,56] Comparing dynamic current-driven, current-driven, and transient response measurements, a waiting time of 3 min was imposed between each sequence of measurement.

*Cell Culture*: Caco-2 cells (DSMZ, ACC 169) were seeded at $1.5 \times 10^5$ cells per insert in a Transwell filter (1.12 $cm^2$, pore size = 0.4 µm). The filter area was reduced to ≈0.16 $cm^2$ using PDMS coating on the backside to lower its ion permeability. The PDMS-modified Transwell filters were coated with collagen, as stated in the literature for enhanced cell attachment, prior to cell seeding. Cells were cultured in EMEM (Invitrogen) with 10% fetal bovine serum (FBS, Invitrogen), 2 mM glutamine (GlutaMax-1, 100×, Invitrogen) and Pen-strep (10 000 µg $mL^{-1}$ penicillin, 10 000 µg $mL^{-1}$ streptomycin, Invitrogen) with a medium change every 2 or 3 days. During the experiments, as well as cell culturing, cells were maintained at 37 °C in a humidified atmosphere with 5% $CO_2$. Four days after seeding cells on Transwell filters of polycarbonate membranes a confluent cell layer is obtained[30,40,41] and the measured TER-value is due to the filter (TER = 10 Ω $cm^2$). Five days after seeding, the TER increases with the presence of TJs to ≈100 Ω $cm^2$ and TER values in the range of 140–700 Ω $cm^2$ are achieved.[31,40–44] As explained by Volpe,[40] the TER depends on various cell culture conditions, such as culturing days, buffer compounds, passage number, etc. In this work, samples with different TER-values were obtained from the same batch. To investigate the DCD approach, "low-resistance" cellular barrier $R$ = 320 Ω $cm^2$, and "high-resistance" cellular barrier $R$ = 640 Ω $cm^2$ were selected. To determine the TER-value, barrier tissue samples were measured using a Volt–Ohm meter EVOM2 from World Precision Instruments.

*Caco-2 Cell Exposure to PLL in Transwell Filter*: Experiments were performed after day 14, corresponding to a TER of ≈500 Ω $cm^2$. The TER was measured with a Volt–Ohm meter EVOM2 from World Precision Instruments. The cells during the experiments were not monitored with the TER because this would require changing the experimental set-up. The cellular barrier with DCD and CD methods was monitored by using the very same experimental set-up without performing manual operations during the measurements. During the monitoring of the cellular barrier, 90 µL PLL dissolved in DI water (122 µM, Sigma-Aldrich) was injected in the apical cell medium and it was verified that the variation of the total ion concentration was negligible. During the whole experiment, the samples were kept in a humified atmosphere with 5% $CO_2$.

*Data Presentation*: The data are presented as one set of experiment. Additional experiments were designed for reproducibility. Among all measurements, the overall behavior (electrical characterization) was reproducible; Software: OriginLab was used for the statistical analysis, and Matlab was used for the data analysis and presentation.

## Supporting Information

Supporting Information is available from the Wiley Online Library or from the author.

## Acknowledgements

The authors acknowledge Dr. Volker Mailänder, MPIP, Universitätsmedizin Mainz. The author F.T. acknowledges the financial support of the European Commission for the project SiMBiT—Single molecule bioelectronic smart system array for clinical testing (HORIZON 2020, Grant Agreement ID: 824946) for partial financial support.

Open Access Funding provided by Universita degli Studi di Brescia within the CRUI-CARE Agreement.

## Conflict of Interest

The authors declare no conflict of interest.

## Data Availability Statement

The data that support the findings of this study are available from the corresponding author upon reasonable request.

## Keywords

biosensors, organic bioelectronics, organic electrochemical transistors, real-time cellular membrane monitoring

Received: October 8, 2022
Revised: January 3, 2023
Published online: February 28, 2023

[1] G. Reyt, P. Ramakrishna, I. Salas-González, S. Fujita, A. Love, D. Tiemessen, C. Lapierre, K. Morreel, M. Calvo-Polanco, P. Flis, N. Geldner, Y. Boursiac, W. Boerjan, M. W. George, G. Castrillo, D. E. Salt, *Nat. Commun.* **2021**, *12*, 2320.
[2] P. Wang, M. Calvo-Polanco, G. Reyt, M. Barberon, C. Champeyroux, V. Santoni, C. Maurel, R. B. Franke, K. Ljung, O. Novak, N. Geldner, Y. Boursiac, D. E. Salt, *Sci. Rep.* **2019**, *9*, 4227.
[3] N. Wettschureck, B. Strilic, S. Offermanns, *Physiol. Rev.* **2019**, *99*, 1467.
[4] C. Chelakkot, J. Ghim, S. H. Ryu, *Exp. Mol. Med.* **2018**, *50*, 1.
[5] C. Zihni, C. Mills, K. Matter, M. S. Balda, *Nat. Rev. Mol. Cell Biol.* **2016**, *17*, 564.
[6] S. Citi, *Science* **2018**, *359*, 1097.
[7] T. Otani, T. P. Nguyen, S. Tokuda, K. Sugihara, T. Sugawara, K. Furuse, T. Miura, K. Ebnet, M. Furuse, *J. Cell Biol.* **2019**, *218*, 3372.
[8] S. L. Barron, J. Saez, R. M. Owens, *Adv. Biol.* **2021**, *5*, 2000624.
[9] L. Kaplan, B. W. Chow, C. Gu, *Nat. Rev. Neurosci.* **2020**, *21*, 416.
[10] U. H. Langen, S. Ayloo, C. Gu, *Annu. Rev. Cell Dev. Biol.* **2019**, *35*, 591.
[11] L. Cacopardo, J. Costa, S. Giusti, L. Buoncompagni, S. Meucci, A. Corti, G. Mattei, A. Ahluwalia, *Biosens. Bioelectron.* **2019**, *140*, 111340.
[12] E. G. B. M. Bossink, M. Zakharova, D. S. De Bruijn, M. Odijk, L. I. Segerink, *Lab Chip* **2021**, *21*, 2040.
[13] S. F. Bint E Naser, H. Su, H. Y. Liu, Z. A. Manzer, Z. Chao, A. Roy, A. M. Pappa, A. Salleo, R. M. Owens, S. Daniel, *ACS Appl. Bio Mater.* **2021**, *4*, 7942.
[14] L. Yuan, H. C. van der Mei, H. J. Busscher, B. W. Peterson, *Front. Microbiol.* **2020**, *11*, 599555.
[15] G. Linz, S. Djeljadini, L. Steinbeck, G. Köse, F. Kiessling, M. Wessling, *Biosens. Bioelectron.* **2020**, *165*, 112345.
[16] D. A. Koutsouras, L. V. Lingstedt, K. Lieberth, J. Reinholz, V. Mailänder, P. W. M. Blom, P. Gkoupidenis, *Adv. Healthcare Mater.* **2019**, *8*, 1901215.
[17] L. H. Jimison, S. A. Tria, D. Khodagholy, M. Gurfinkel, E. Lanzarini, A. Hama, G. G. Malliaras, R. M. Owens, *Adv. Mater.* **2012**, *24*, 5919.
[18] F. Santoro, C. Lubrano, G. M. Matrone, G. Iaconis, *ACS Nano* **2020**, *14*, 12271.
[19] C. Pitsalidis, A. M. Pappa, A. J. Boys, Y. Fu, C. M. Moysidou, D. van Niekerk, J. Saez, A. Savva, D. Iandolo, R. M. Owens, *Chem. Rev.* **2022**, *122*, 4700.
[20] J. Rivnay, S. Inal, A. Salleo, R. M. Owens, M. Berggren, G. G. Malliaras, *Nat. Rev. Mater.* **2018**, *3*, 17086.
[21] P. Romele, M. Ghittorelli, Z. M. Kovács-Vajna, F. Torricelli, *Nat. Commun.* **2019**, *10*, 3044.
[22] F. Torricelli, D. Z. Adrahtas, Z. Bao, M. Berggren, F. Biscarini, A. Bonfiglio, C. A. Bortolotti, C. D. Frisbie, E. Macchia, G. G. Malliaras, I. McCulloch, M. Moser, T.-Q. Nguyen, R. M. Owens, A. Salleo, A. Spanu, L. Torsi, *Nat. Rev. Methods Primers* **2021**, *1*, 66.
[23] R. Granelli, I. Alessandri, P. Gkoupidenis, I. Vassalini, Z. M. Kovács-Vajna, P. W. M. Blom, F. Torricelli, *Small* **2022**, *18*, 2108077.
[24] D. A. Koutsouras, F. Torricelli, P. W. M. Blom, *Adv. Electron. Mater.* **2022**, https://doi.org/10.1002/aelm.202200868.
[25] M. Ramuz, K. Margita, A. Hama, P. Leleux, J. Rivnay, I. Bazin, R. M. Owens, *ChemPhysChem* **2015**, *16*, 1210.
[26] M. Ramuz, A. Hama, J. Rivnay, P. Leleux, R. M. Owens, *J. Mater. Chem. B* **2015**, *3*, 5971.
[27] F. Decataldo, M. Barbalinardo, M. Tessarolo, V. Vurro, M. Calienni, D. Gentili, F. Valle, M. Cavallini, B. Fraboni, *Adv. Mater. Technol.* **2019**, *4*, 1900207.
[28] C. Yao, C. Xie, P. Lin, F. Yan, P. Huang, I.-M. Hsing, *Adv. Mater.* **2013**, *25*, 6575.
[29] A. Romeo, G. Tarabella, P. D'Angelo, C. Caffarra, D. Cretella, R. Alfieri, P. G. Petronini, S. Iannotta, *Biosens. Bioelectron.* **2015**, *68*, 791.
[30] L. V. Lingstedt, M. Ghittorelli, M. Brückner, J. Reinholz, N. I. Crăciun, F. Torricelli, V. Mailänder, P. Gkoupidenis, P. W. M. Blom, *Adv. Healthcare Mater.* **2019**, *8*, 1900128.
[31] K. Lieberth, P. Romele, F. Torricelli, D. A. Koutsouras, M. Brückner, V. Mailänder, P. Gkoupidenis, P. W. M. Blom, *Adv. Healthcare Mater.* **2021**, *10*, 2100845.
[32] K. Lieberth, M. Brückner, F. Torricelli, V. Mailänder, P. Gkoupidenis, P. W. M. Blom, *Adv. Mater. Technol.* **2021**, *6*, 2000940.
[33] V. Kaphle, S. Liu, C. M. Keum, B. Lüssem, *Phys. Status Solidi A* **2018**, *215*, 1800631.
[34] V. Kaphle, P. R. Paudel, D. Dahal, R. K. Radha Krishnan, B. Lüssem, *Nat. Commun.* **2020**, *11*, 2515.
[35] A. F. Paterson, A. Savva, S. Wustoni, L. Tsetseris, B. D. Paulsen, H. Faber, A. H. Emwas, X. Chen, G. Nikiforidis, T. C. Hidalgo, M. Moser, I. P. Maria, J. Rivnay, I. McCulloch, T. D. Anthopoulos, S. Inal, *Nat. Commun.* **2020**, *11*, 3004.
[36] G. C. Faria, D. T. Duong, A. Salleo, *Org. Electron.* **2017**, *45*, 215.
[37] A. Giovannitti, R. B. Rashid, Q. Thiburce, B. D. Paulsen, C. Cendra, K. Thorley, D. Moia, J. T. Mefford, D. Hanifi, D. Weiyuan, M. Moser, A. Salleo, J. Nelson, I. McCulloch, J. Rivnay, *Adv. Mater.* **2020**, *32*, 1908047.
[38] M. P. Ferro, L. Leclerc, M. Sleiman, B. Marchiori, J. Pourchez, R. M. Owens, M. Ramuz, *Adv. Biosyst.* **2019**, *3*, 1800249.
[39] F. Decataldo, M. Barbalinardo, D. Gentili, M. Tessarolo, M. Calienni, M. Cavallini, B. Fraboni, *Adv. Biosyst.* **2020**, *4*, 1900204.
[40] D. A. Volpe, *J. Pharm. Sci.* **2008**, *97*, 712.
[41] J. Reinholz, C. Diesler, S. Schöttler, M. Kokkinopoulou, S. Ritz, K. Landfester, V. Mailänder, *Acta Biomater.* **2018**, *71*, 432.
[42] P. Artursson, C. Magnusson, *J. Pharm. Sci.* **1990**, *79*, 595.
[43] S. Tria, L. H. Jimison, A. Hama, M. Bongo, R. M. Owens, *Biosensors* **2013**, *3*, 44.
[44] M. Ramuz, A. Hama, M. Huerta, J. Rivnay, P. Leleux, R. M. Owens, *Adv. Mater.* **2014**, *26*, 7083.
[45] W. Shin, H. J. Kim, *Nat. Protoc.* **2022**, *17*, 910.
[46] M. C. Valenzano, K. DiGuilio, J. Mercado, M. Teter, J. To, B. Ferraro, B. Mixson, I. Manley, V. Baker, B. A. Moore, J. Wertheimer, J. M. Mullin, *PLoS One* **2015**, *10*, 0133926.
[47] M. Ghittorelli, L. Lingstedt, P. Romele, N. I. Crăciun, Z. M. Kovács-Vajna, P. W. M. Blom, F. Torricelli, *Nat. Commun.* **2018**, *9*, 1441.
[48] S. A. Tria, M. Ramuz, M. Huerta, P. Leleux, J. Rivnay, L. H. Jimison, A. Hama, G. G. Malliaras, R. M. Owens, *Adv. Healthcare Mater.* **2014**, *3*, 1053.
[49] K. B. Riaz Ahmed, A. M. Nagy, R. P. Brown, Q. Zhang, S. G. Malghan, P. L. Goering, *Toxicol. In Vitro* **2017**, *38*, 179.
[50] C. Y. Yang, M. A. Stoeckel, T. P. Ruoko, H. Y. Wu, X. Liu, N. B. Kolhe, Z. Wu, Y. Puttisong, C. Musumeci, M. Massetti, H. Sun, K. Xu, D. Tu, W. M. Chen, H. Y. Woo, M. Fahlman, S. A. Jenekhe, M. Berggren, S. Fabiano, *Nat. Commun.* **2021**, *12*, 2354.

[51] R. B. Rashid, W. Du, S. Griggs, I. P. Maria, I. McCulloch, J. Rivnay, *Sci. Adv.* **2021**, *7*, 1055.
[52] L. Huang, Z. Wang, J. Chen, B. Wang, Y. Chen, W. Huang, L. Chi, T. J. Marks, A. Facchetti, *Adv. Mater.* **2021**, *33*, 2007041.
[53] M. Moser, T. C. Hidalgo, J. Surgailis, J. Gladisch, S. Ghosh, R. Sheelamanthula, Q. Thiburce, A. Giovannitti, A. Salleo, N. Gasparini, A. Wadsworth, I. Zozoulenko, M. Berggren, E. Stavrinidou, S. Inal, I. McCulloch, *Adv. Mater.* **2020**, *32*, 2002748.
[54] D. A. Koutsouras, M. H. Amiri, P. W. M. Blom, F. Torricelli, K. Asadi, P. Gkoupidenis, *Adv. Funct. Mater.* **2021**, *31*, 2011013.
[55] L. V. Lingstedt, M. Ghittorelli, H. Lu, D. A. Koutsouras, T. Marszalek, F. Torricelli, N. I. Crăciun, P. Gkoupidenis, P. W. M. Blom, *Adv. Electron. Mater.* **2019**, *5*, 1800804.
[56] F. Decataldo, L. Grumiro, M. M. Marino, F. Faccin, C. Giovannini, M. Brandolini, G. Dirani, F. Taddei, D. Lelli, M. Tessarolo, M. Calienni, C. Cacciotto, A. Lavazza, B. Fraboni, A. Scagliarini, V. Sambri, *Commun. Mater.* **2022**, *3*, 5.